Moving Valve Controlled Transient Cavitation Dynamics in a Contracting Nozzle: A Lattice Boltzmann Simulation Study

T.P. Luo[1,2], J. Xia[*3]

[1]Beijing Institute of Aerospace Testing Technology, Beijing 100074, China
[2]Beijing Engineering Research Center of Aerospace Testing Technology and Equipment, Beijing 100074, China
[3]Department of Mechanical and Aerospace Engineering & Institute of Energy Futures, Brunel University London, Uxbridge UB8 3PH, UK
*Corresponding author email: jun.xia@brunel.ac.uk

Abstract

In the present study, a two-dimensional low-Reynolds-number cavitating contracting-nozzle flow interacting with a moving valve is simulated using the lattice Boltzmann (LB) method. The Bhatnagar-Gross-Krook algorithm coupled with the immersed boundary method and an improved pseudo-potential multiphase flow model has been further developed based on the open-source LB code PALABOS. In order to improve the pseudo-potential model on its limitation of the density ratio, the Carnahan-Starling equation of state is incorporated together with the exact difference method force scheme and an upgraded interaction force term. Using PALABOS, cavitation in a contracting nozzle is simulated for a whole cycle of the valve motion. It is found that cavitation dynamics, including interface conditions, cavitation bubble distributions, inside-bubble vapour-phase flow fields, are all distinctly different at different fuel mass flow rates when the flow path is widely open and completely shut by the valve.

Keywords

Cavitation; Valve; Lattice Boltzmann; Immersed Boundary; Density Ratio

Introduction

Cavitation in liquid-fuel injectors is a widely impactive problem in spray engineering. Its interaction with the moving needle valve controls the fuel mass flow rate. Therefore the cavitating flow dynamics internal to the injector nozzle has significant impact on spray dynamics, combustion performance and emissions in aero and auto combustion engines by dictating the upstream boundary conditions at the nozzle exit. Despite its key role, internal cavitating flow dynamics under the impact of the moving needle valve remains poorly understood due to the difficulty both in measurement and computational approaches.

The lattice Boltzmann method has attracted great attention over the past few decades due to its simple scheme and the easement of dealing with complex or moving geometry [1]. In addition, the mesoscopic nature of the LB method makes it suitable for multiphase flow problems, especially for cavitation or phase transition problems, since phases are not distinguished in the LB method. To deal with moving geometry, bounce-back schemes and the immersed boundary method can be used in the LB method. The immersed boundary method [2, 3] in general provides more stable solutions with an overall comparable accuracy and more convenience when dealing with complex geometry [4]. Its idea is to represent the effect of the boundary by a force applying to the neighbouring region of the (fluid-moving) geometry interface. The common feature that both the LB and immersed boundary methods are usually discretised on regular Cartesian meshes makes it feasible for the two approaches to easily and effectively cooperate.

The LB multiphase flow models mainly include the pseudo-potential [5, 6, 7] and free-energy [8] models. Although the latter is thermodynamically consistent, it is usually difficult to achieve high density ratios as in realistic engineering gas-liquid flow and suffers numerical instability. Overall, the pseudo-potential model, which employs a pseudo-potential function to account for

nonlocal particle interactions, is widely used due to its simplicity and versatility. The original pseudo-potential model suffers from its inherent limitations including the relatively large spurious velocity currents, thermodynamic inconsistency, a low density ratio and the dependence of the surface tension and density ratio on the viscosity. In recent years, further research on this model has focused on increasing tolerable density ratios while decreasing spurious velocities, including incorporating a more realistic EOS into the original model [9, 10], increasing the isotropy order of the interaction force [11], incorporating an improved interaction force [12, 13] and force schemes [14, 15, 16] into the LB framework.

In the present study, we further developed PALABOS for an upgraded pseudo-potential model to cooperate with the immersed boundary method in the code. The pseudo-potential model is improved by incorporating the Carnahan-Starling (C-S) equation of state, the exact difference method force scheme and an upgraded interaction force term. Using PALABOS, an internal cavitating contracting-nozzle flow interacting with a moving valve was simulated. Transient cavitation phenomena during a whole cycle of the valve motion are revealed. Distinctly different cavitating flow dynamics under different mass flow rates, especially between the time instants when the flow path is widely open and completely shut off by the valve, is discussed.

Lattice Boltzmann method

The LB method is based on the Boltzmann equation and simulates flow transport by the evolution of the distribution functions. The widely used Bhatnagar-Gross-Krook (BGK) approximation [1] is employed in the present study. The BGK method is based on the development of discrete molecular velocity distribution functions on uniform Cartesian lattices. The velocity distribution functions can be written as

$$f_i(\mathbf{x}+\mathbf{e}_i\delta t, t+\delta t) - f_i(\mathbf{x},t) = -\frac{\delta t}{\tau}[f_i(\mathbf{x},t) - f_i^{\mathrm{eq}}(\mathbf{x},t)] + F_i(\mathbf{x},t)\delta t\ , \tag{1}$$

$$f_i^{\mathrm{eq}} = \omega_i \rho \left[1 + \frac{\mathbf{u}\cdot\mathbf{e}_i}{c_{\mathrm{s}}^2} + \frac{(\mathbf{u}\cdot\mathbf{e}_i)^2}{2c_{\mathrm{s}}^4} - \frac{\mathbf{u}\cdot\mathbf{u}}{2c_{\mathrm{s}}^2}\right]\ , \tag{2}$$

$$\rho = \sum_i f_i,\quad \rho\mathbf{u} = \sum_i f_i\mathbf{e}_i + \frac{\mathbf{F}\delta t}{2},\quad \nu = (\tau - 0.5)c_{\mathrm{s}}^2\delta t, \tag{3}$$

where f and f^{eq} are the distribution function and equilibrium distribution function, respectively; the index i defines the vector of the discrete molecular velocities; ω is the weight factor for different speed vectors; τ and ν are the relaxation time and kinematic viscosity, respectively; c_{s} is the lattice speed of sound, and its squared value usually equals $1/3$; $\mathbf{u}$ and ρ are the macroscopic velocity and density, respectively; $\mathbf{x}$ and $\mathbf{e}$ are the spatial location and base velocity in the LB method, respectively; $\mathbf{F}$ is the external force. To improve the numerical stability of the pseudo-potential model, the exact difference scheme [14] is adopted and the relationship between $\mathbf{F}$ and F_i is calculated as $F_i(\mathbf{x},t) = f_i^{\mathrm{eq}}(\rho, \mathbf{u}^{\mathrm{eq}} + \mathbf{F}\delta t/\rho) - f_i^{\mathrm{eq}}(\rho, \mathbf{u}^{\mathrm{eq}})$, where $\mathbf{u}^{\mathrm{eq}} = \Sigma_i f_i\mathbf{e}_i/\rho$.

In the present study, the external force $\mathbf{F}$ consists of contributions from $\mathbf{f}^{\mathrm{SC}}$ due to pseudo-potential interactions in the gas-liquid flow and the immersed boundary force $\mathbf{f}_{\mathrm{IB}}$. Due to the page limit, refer to [17] for details of implementing the immersed boundary method in the LB framework, where Dütsch's measurements [18] of an oscillating cylinder in liquid has been used to validate the coupled numerical algorithms. The interaction force $\mathbf{f}^{\mathrm{SC}}$ originally proposed by Shan and Chen [5, 6, 7] can be written as

$$\mathbf{f}^{\mathrm{SC}}(\mathbf{x},t) = -\beta c_0\psi(\mathbf{x})G\nabla\psi(\mathbf{x}) - \frac{1-\beta}{2}c_0 G\nabla\psi^2(\mathbf{x}), \tag{4}$$

where β is a weighting factor; G is a scalar that controls the strength of the interaction force; $c_0 = 6$ for D2Q9. A discretised form of Eq. 4 is implemented in the code as

$$\mathbf{f}^{\mathrm{SC}}(\mathbf{x},t) = -\beta\psi(\mathbf{x})G\sum_i \omega(|\mathbf{e}_i|^2)\psi(\mathbf{x}+\mathbf{e}_i\delta t)\mathbf{e}_i\delta t - \frac{1-\beta}{2}G\sum_i \omega(|\mathbf{e}_i|^2)\psi^2(\mathbf{x}+\mathbf{e}_i\delta t)\mathbf{e}_i\delta t. \tag{5}$$

$\omega(1) = 1/3$ and $\omega(2) = 1/12$ for D2Q9. To incorporate a realistic EOS [9], the pseudo-potential function is given by

$$\psi = \sqrt{\frac{2(P_{\mathrm{EOS}} - \rho c_{\mathrm{s}}^2)}{Gc^2}}, \tag{6}$$

where $c = 1$ is the lattice speed; G is set to be -1 to keep the square root value positive; P_{EOS} is determined by the Carnahan-Starling EOS:

$$P_{\mathrm{EOS}} = \rho RT \frac{1 + b\rho/4 + (b\rho/4)^2 - (b\rho/4)^3}{(1 - b\rho/4)^3} - a\rho^2, \tag{7}$$

where $a = 0.4963R^2T_{\mathrm{c}}^2/P_{\mathrm{c}}$ and $b = 0.18727RT_{\mathrm{c}}/P_{\mathrm{c}}$. T_{c} and P_{c} are the critical temperature and pressure, respectively. The temperature T and T_{c} are both constants in the present study. a is vitally important for the stability of this modified model. Reducing a increases the interface thickness and thus reduces the spurious currents [13]. In this study, $a = 0.13$, $b = 4$ and $R = 1$. The weighting factor β in Eq. 5 for the C-S EOS is set to be 1.315.

The thermodynamic consistency of the improved pseudo-potential model has been evaluated against Maxwell construction. A liquid/vapour mixture with the density ratio up to $\sim$ 2,400 where T/T_{c} = 0.45 can be accurately reproduced [17]. In addition, a co-current flow in a two-dimensional (2D) channel driven by an external force is simulated to demonstrate the accuracy of the improved pseudo-potential model in realistic gas-liquid two-phase flow. The LB results agree well with the analytical solutions for three density-ratio cases $\rho_{\mathrm{L}}/\rho_{\mathrm{G}}$ at 100, 1,000 and 2,400 [17]. Cavitating flow simulations have also been performed, using a similar configuration to that in [19, 20]. The discharge coefficient, which is defined as the ratio of the actual mass flow rate to the ideal mass flow rate of the fluid passing through the nozzle, agrees reasonably well with published experimental data [21, 22, 23].

Cavitating contracting-nozzle flow interacting with a moving valve

In this study, a moving valve is introduced into the contracting-nozzle configuration, as shown in Fig. 1, to make a further step towards a realistic liquid-fuel injector, and more broadly, the working-liquid injectors in a variety of spraying devices.

The initial location of the valve is set to be 50 lattices into the domain in x direction. The motion algorithm of the valve follows a cosine function, i.e. $U(t) = -\pi/250\cos(\pi t/25000 + \pi/2)$. With this algorithm, it takes 50,000 time steps for the valve to complete one cycle (see Fig. 2). Note since the times step $\Delta t = 1$, the number $N_{\Delta t}$ of elapsed time steps is equivalently the present simulation time, i.e. $t = 50,000$ at $N_{\Delta t} = 50,000$.

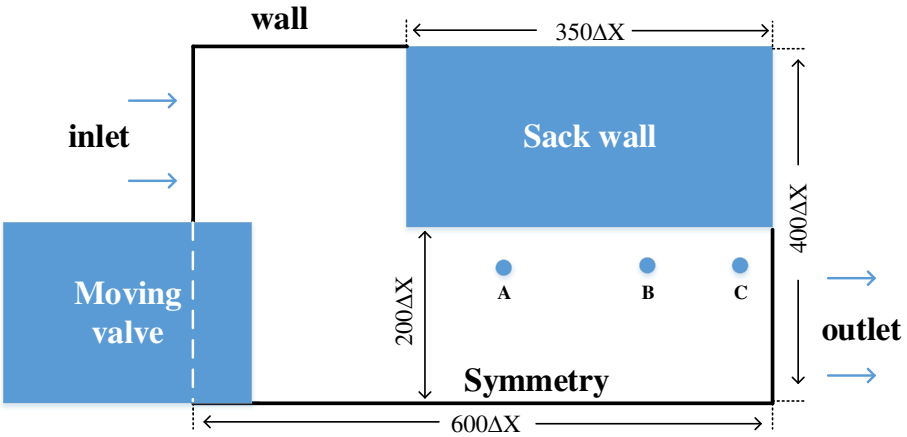

Figure 1. Sketch of a contracting cavitation nozzle that interacts with a moving valve. Coordinates of the three probes: A(350,150), B(480,150) and C(580,150).

The Zou/He-type [24] pressure boundaries are imposed at both the inlet and outlet. The bottom boundary of the simulation domain is set to be symmetric. The liquid/gas density ratio

is 1,000. At the inlet, the density is set to be 0.53, while 0.4614 at the outlet. Taking the moving valve out of consideration, strong cavitation will occur in the whole contracting nozzle in this case, according to the cavitation number K [19, 20]. K is defined as $K = (P_{\rm in} - P_{\rm v})/(P_{\rm in} - P_{\rm out})$, where $P_{\rm in}$ is the total pressure at the nozzle inlet, $P_{\rm out}$ is the static pressure at the outlet and $P_{\rm v}$ is the saturation vapour pressure. When K diminishes to a specific value, cavitation will occur. At the intersection of the moving valve and the inlet which is indicated as a dashed line in the moving block in Fig. 1, zero velocity and the same value of density as that at the inlet (0.53) are simultaneously set to prevent non-physical mass from entering the computational domain on the one hand, and to keep the numerical simulation stable on the other. Before starting the unsteady simulation, an initial flow field is obtained by fixing the position of the valve. After $\sim$ 16,000 time steps, a converged flow field is attained, and a stable cavitation region emerges in the nozzle. This flow field is used as the initial condition for the subsequent simulation with the valve moving. We use a "cavitation region" in the present study to indicate a region where the fluid density drops abruptly. As will be shown below, distinctly different distribution profiles of the fluid density can be found in a seemingly similar cavitation region, depending on the local flow dynamics which is controlled by the moving valve. The viscosity is set to be 1.0. The initial Reynolds number is $\sim$ 46, and the Reynolds number of the valve is $\sim$ 2.5.

Figure 2 shows the density contours, superimposed with flow velocity vectors, at different time instants during a whole cycle of the valve motion. The 10-based-logarithmic scale has been used for the density to better distinguish low densities inside the cavitation region. At t = 0, a stable cavitation zone extends towards the outlet, which is consistent with what is expected from the K criterion. A low-density small area emerges just under the sack wall as the valve moves towards the nozzle, and coalesces with the existing stable cavitation region at $t = 9,500$. At t = 17,500, the velocity magnitudes of the flow field significantly reduce (see the velocity vectors) since the valve is shutting off the flow path, and the cavitation region tends to become wider in the y direction due to a reduction of the flow velocity in the x direction and thus a reduction of the flow shear. At t = 25,000 when the valve reaches its rightmost location and so the flow path is completely shut, the cavitation region shows an elliptic shape, with its major axis pointing towards upper left under the remaining influence of flow shear. It should also be noted that in previous time instants the fluid density monotonically decreases with orders of magnitude towards inside the core of the cavitation region, which would indicate a single large cavitation bubble at the core. At $t = 25,000$, on the other hand, small low-density islands distribute inside the cavitation region, as illustrated by the two small brown regions in Fig. 2d, which would imply a possibility of multiple coexisting small bubbles in the area. At $t = 33,000$, the cavitation region shrinks as the fluid is reentering the contracting nozzle. Meanwhile the very-low-density brown regions shown in Fig. 2d disappear, implying an increase of the average density in the shrinking cavitation region. The shrunk cavitation region has moved towards left due to the traction effects of the valve, which now moves away from the contracting nozzle. The major axis of the elliptic cavitation region now points towards upper right under the valve traction when the flow shear is still not strong. $t = 34,500$ is a unique time instant when the cavitation region appears most circular under the competition between the traction due to the leaving valve and gradually strengthening shearing flow through the flow path opened by the valve. At $t = 35,000$, which corresponds to 70% of a complete cycle of the valve motion, cavitation disappears. The low local fluid velocity and a relatively high static pressure cannot maintain a low-density cavitation region. At t = 44,000 when a cycle of the valve motion completes 88%, the nozzle flow has accelerated to a state close to that at the initial time instant, and a new low-density small region reemerges and grows towards the outlet. At t = 50,000, a whole cycle completes, and the cavitation region recovers its initial state as shown in Fig. 2a.

The density variations at three probing locations are monitored during the whole cycle, as shown in Fig. 3. The three probes (350,150), (480,150) and (580,150) are located at upstream, the core and the trailing edge of the cavitation region, respectively, as shown in Fig. 1 by Point A, B and C. The black line shows that considerable density fluctuations occur before t = 15,000 at A(350,150), indicating continuous rupture and reconstruction of a cavitation bubble;

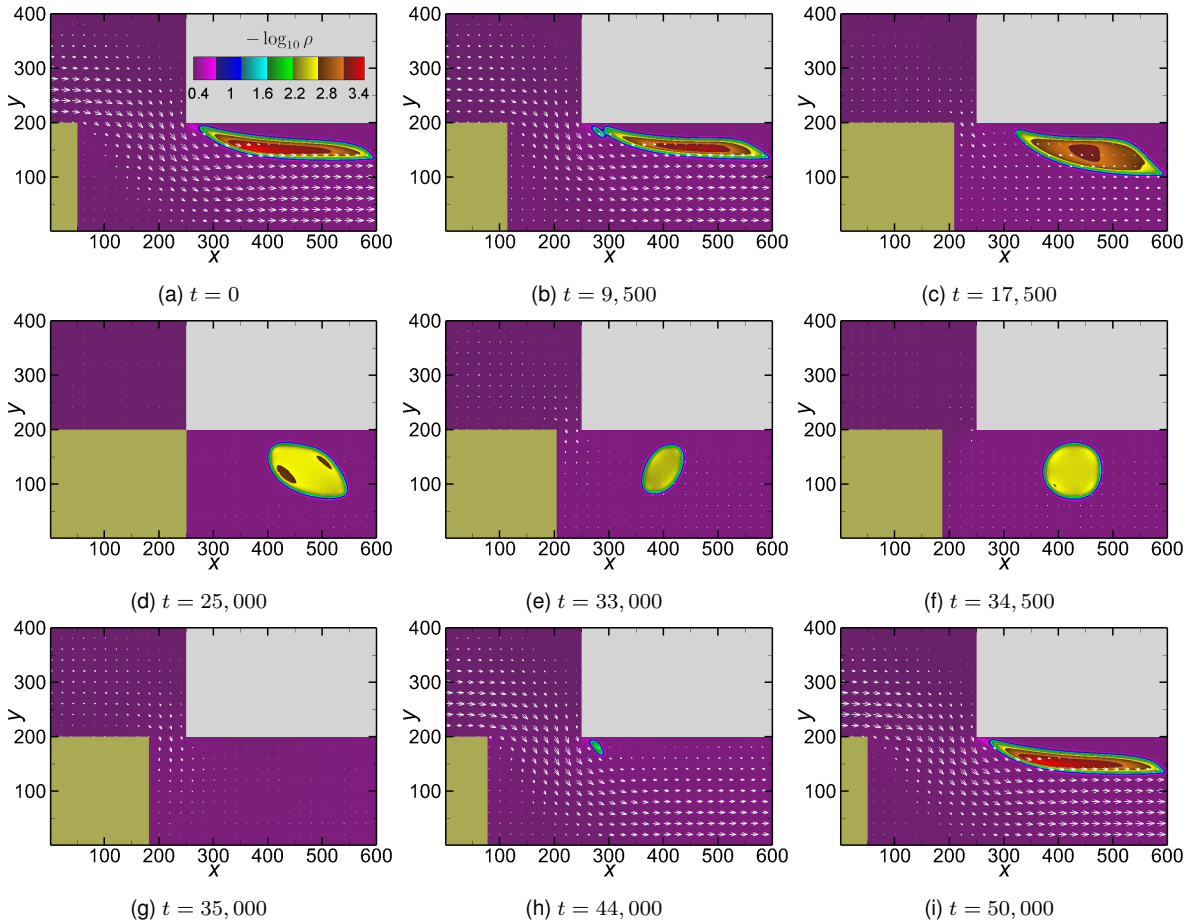

Figure 2. Density contours and velocity vectors at different time instants during one moving-valve cycle. $-\log_{10}\rho \in [0.25, 3.59] \Leftrightarrow \rho \in [0.00026, 0.56] \Leftrightarrow \rho^* \in [0.41, 899.23]$ kg / m^3. $t = 50,000 \Leftrightarrow t^* = 5 \times 10^{-6}$ s.

the density rises to the liquid equilibrium value between $t \approx 17,000$ and 45,000, which indicates the local fluid remains liquid and the cavitation region is away from this location during this period of time; after t = 45,000, the density decreases dramatically towards its initial value at t = 50,000. At B(480,150), the red line shows the density oscillates around its equilibrium vapour value before $t \approx 15,000$; due to the valve's compression effect, the density becomes slightly higher between t = 15,000 and 30,000. However, the vapour-phase state is still maintained; afterwards, the density rises rapidly towards the liquid value, which corresponds to the shrinking and disappearing process of the cavitation region in Fig. 2. At C(580,150) (the blue line), the density is equal to its equilibrium liquid value most of the time, since the cavitation region shrinks and moves towards upstream, as shown in Fig. 2.

More detailed analysis is now given on cavitation dynamics under different flow conditions when the flow path is widely open and completely shut by the valve. At $t = 9,500$, the valve has started to move towards the contracting nozzle, while the flow path still remains widely open. A magnified view of the cavitation region is shown in Fig. 4a. Note the x to y ratio has been enlarged to $2:1$ to clearly show the information. Here the density of the red line is $0.455 \sim \rho_0$, which is slightly lower than the initial liquid density $\rho_0 = 0.46$. The density of the pink lines is $0.046 = 10^{-1}\rho_0$. It is therefore reasonable to approximate the region between the red and pink contour lines, more specifically the green belt, as the interface regions between liquid and gas. Encircled by pink contour lines are cavitating gas bubbles, as shown by yellow floods in Fig. 4a. The other contour lines shown in the figure denote densities of $0.0046 = 10^{-2}\rho_0$, $0.001 \sim \mathcal{O}(10^{-2})\rho_0$ and $0.00055 \sim \mathcal{O}(10^{-3})\rho_0$. It can be seen that in the cavitating region, the fluid density monotonically decreases towards the core region. The flow is outgoing at the outlet boundary, as shown in Fig. 4a. A strong shear layer exists in the liquid-gas-liquid

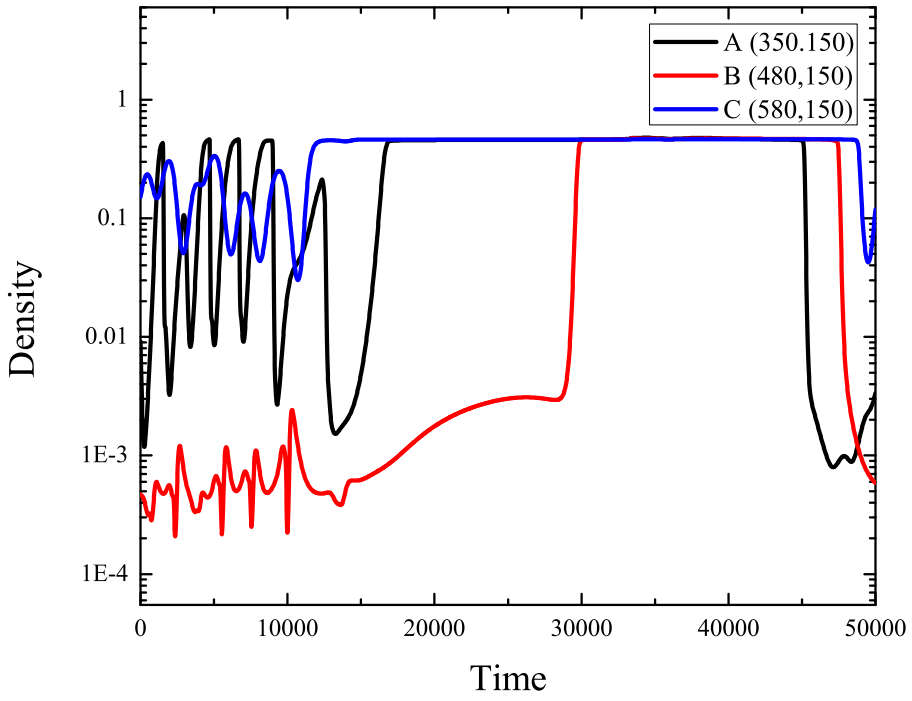

Figure 3. Density variations at three monitored locations. $\rho = 1 \Leftrightarrow \rho^* = 1612.47$ kg / m^3. $t = 50,000 \Leftrightarrow t^* = 5 \times 10^{-6}$ s.

region, but there is no abrupt changes to velocities (no/weak velocity jumps) from the liquid to the gas, although the velocity gradient normal to the interface direction is considerable. See the interface regions between the red and pink contour lines. The velocity vectors seem to align well with the tangential directions of the density contour lines. Therefore under the current working condition, the flow is taking the dominant role in controlling the cavitation.

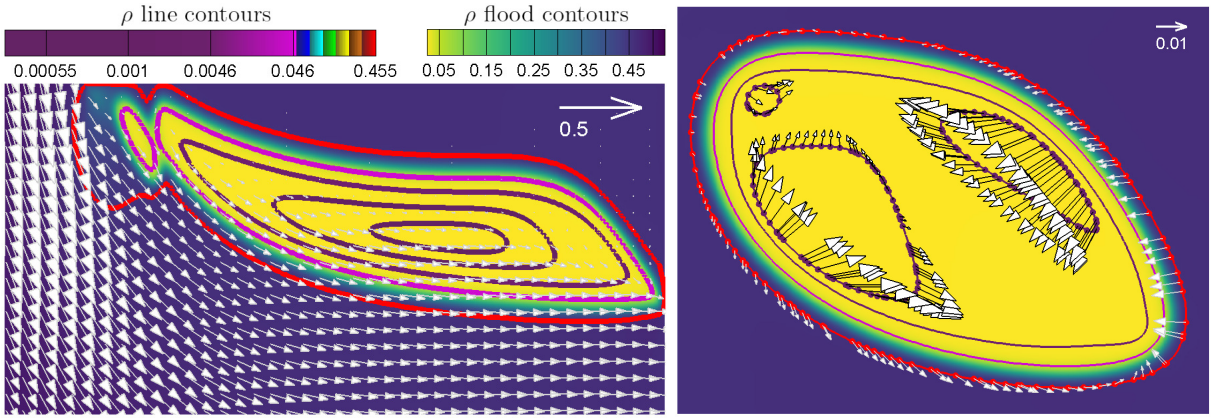

(a) Density and velocity fields at $t = 9,500$ when the valve is shutting off but still widely open.

(b) Velocity vectors on $\rho = 0.455$ and 0.00253 at $t = 25,000$ when the valve completely shuts off the flow path.

Figure 4. Comparison of density and velocity fields between two time instants when the flow path is open and shut. Both line and flood contours are presented for density ρ using different colour maps.

On the other hand, at $t = 25,000$ the valve has just reached its rightmost location and therefore the flow path is completely shut off. As shown in Fig. 4b, the characteristics of the cavitation bubble and flow at this time instant are significantly different from those at $t = 9,500$. First the difference of velocity magnitudes between the two time instants should be noted (also see Fig. 2b and Fig. 2d). In Fig. 4b, velocity vectors are shown on the red contour line where $\rho = 0.455 \sim \rho_0$, i.e. on the liquid side of the interface, and on brown contour lines where $\rho = 0.00253 \sim \mathcal{O}(10^{-2})\rho_0$. In contrast to Fig. 4a, there is an inward flow from the outlet

boundary, which is more clearly shown by the streamlines in Fig. 5a. In spray combustion as an important engineering application of cavitating spraying, flashback into the injector nozzle after the needle valve shuts the supply of high-pressure liquid fuel has been well recognised to be important for accurately controlling the fuel mass flow rate and avoiding adverse impact of high-temperature burned products on the injector nozzle.

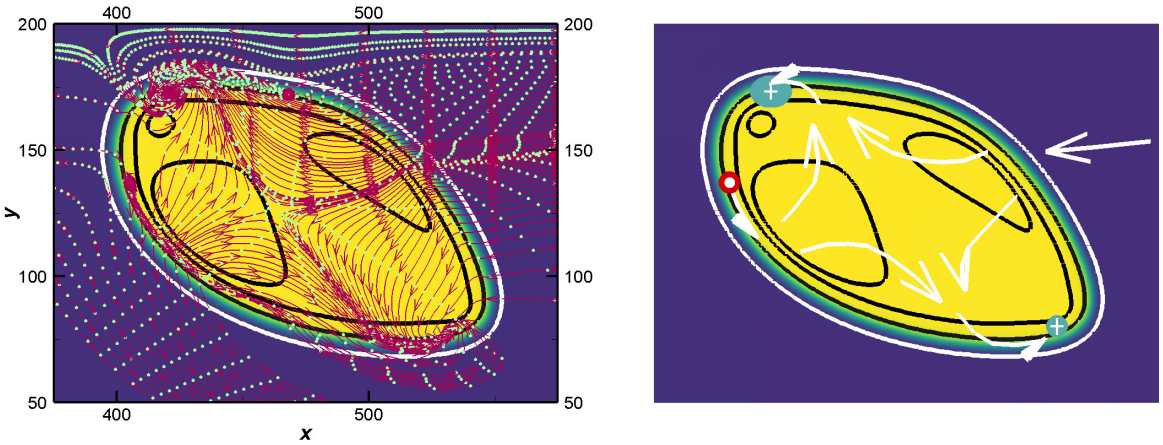

(a) Streamlines on density contours

(b) Illustration of streamline distribution inside cavitation bubble

Figure 5. Streamlines at $t = 25,000$ when the flow channel is completely shut off by the valve.

Different from the negligible liquid flow velocities in regions towards the valve side, inside the interface approximately represented by the green belt the gas-phase velocity is still considerable, as shown by the velocity vectors on the $\rho = 0.00253$ contour lines. Towards the outlet boundary, the difference is in magnitudes, with a higher gas-phase speed. Towards the valve side, the difference is in both magnitude and direction. Overall, there is a big velocity jump on the interface between the two phases.

To better show the flow characteristics around and inside the remaining cavitating bubble, Fig. 5a shows a set of streamlines on the density contours. The rectangular area covering the white (shown as red in Fig. 4b) density contour $\rho = 0.455$ is identified. The two diagonal lines of the rectangle have been used to create 50 seed points on each line to generate the streamlines that can nicely cover the whole bubble with all flow characteristics properly shown. The spacing between neighbouring green markers on one streamline indicates the magnitude of the local velocity. Therefore close to the bottom of the sack wall $y = 200$, there is virtually no flow. All the streamlines entering the plot from the left side come through a narrow opening around $[x, y] = [250, 200]$ where the valve meets the sack wall. All the streamlines from the right side are back fed from the outlet boundary.

It can be seen that there are one streamline source and two streamline sinks at the gas-liquid interface, as indicated in Fig. 5b. One streamline sink is close to one of the three density contour lines $\rho = 0.00253$ located on the top of the cavitation bubble, while the other is located on the lower right side of the bubble. The streamline source is found close to the leftmost part of the bubble. The streamlines inside the bubble march towards the two sinks if they have external sources or generated by the internal source, as shown in Fig. 5a and illustrated in Fig. 5b.

Conclusions

In the present study, a 2D low-Reynolds-number cavitating flow interacting with a moving valve has been investigated using lattice Boltzmann methods based on the further developed open-source code PALABOS. With the cooperation of the immersed boundary method and an improved pseudo-potential model, which incorporates the Carnahan-Starling equation of state and an upgraded interaction force term, LB simulation of internal transient cavitating flow in a contracting channel interacting with a moving valve has been performed. Distinctly different cavitation dynamics at different valve openings has been discovered. When the flow path is still

widely open as the valve moves towards the contracting nozzle, the cavitation region evolves from a sheared layer towards an ecliptic shape. Inside the cavitation region, the fluid density decrease monotonically towards inside, so a single big cavitation bubble exists at the core. On the other hand, when the incoming flow path is completely shut by the valve, distributed low-density islands are found inside the cavitation region, implying a scatter of small bubbles in the cavitation region. Back-flow at the nozzle exit imposes an important impact on inside-bubble flow. The velocity jumps on the gas-liquid interface are considerable. Two sinks and one source are found for streamlines inside the cavitation region. With the valve gradually opening again, cavitation disappears under the competing impact of the traction effects of the moving-away valve and strengthening incoming-flow shear. Finally, a small low-density area reemerges under the tip of the sack wall that faces the incoming flow, gradually grows and recovers the initial cavitation region which extends towards the outlet as the flow path is widely open.

Acknowledgements

This paper is adapted from [17]. Financial support from the China Scholarship Council (No. CSC201804980019), the Royal Society (IES\R3\193152) and the Engineering and Physical Sciences Research Council (EPSRC; EP/T033940/1) of the UK is gratefully acknowledged.

References

[1] Chen, S., Doolen, G., 1998. *Annu. Rev. Fluid Mech.,* ***30***, pp. 329–364.
[2] Peskin, C., 1972. *J. Comput. Phys.,* ***10***(2), pp. 252–271.
[3] Peskin, C., 1977. *J. Comput. Phys.,* ***25***(3), pp. 220–252.
[4] De Rosis, A., Ubertini, S., Ubertini, F., 2014. *J. Sci. Comput.,* ***61***(3), pp. 477–489.
[5] Shan, X., Chen, H., 1993. *Phys. Rev. E,* ***47***(3), pp. 1815–1819.
[6] Shan, X., Chen, H., 1994. *Phys. Rev. E,* ***49***(4, A), pp. 2941–2948.
[7] Shan, X., Doolen, G., 1995. *J. Stat. Phys.,* ***81***(1-2), pp. 379–393.
[8] Swift, M., Orlandini, E., Osborn, W., Yeomans, J., 1996. *Phys. Rev. E,* ***54***(5), pp. 5041–5052.
[9] Yuan, P., Schaefer, L., 2006. *Phys. Fluids,* ***18***(4), article no. 042101.
[10] Zhang, J., Tian, F., 2008. *EPL,* ***81***(6), article no. 66005.
[11] Peng, C., Ayala, L. F., Ayala, O. M., Wang, L.-P., 2019. *Comput. Fluids,* ***191***, article no. UNSP 104257.
[12] Gong, S., Cheng, P., 2012. *Comput. Fluids,* ***53***, pp. 93–104.
[13] Kharmiani, S. F., Niazmand, H., Passandideh-Fard, M., 2019. *J. Stat. Phys.,* ***175***(1), pp. 47–70.
[14] Kupershtokh, A. L., Medvedev, D. A., Karpov, D. I., 2009. *Comput. Math. Appl.,* ***58***(5), pp. 965–974.
[15] Huang, H., Krafczyk, M., Lu, X., 2011. *Phys. Rev. E,* ***84***(4, 2), article no. 046710.
[16] Li, Q., Luo, K. H., Li, X. J., 2012. *Phys. Rev. E,* ***86***(1, 2), article no. 016709.
[17] Luo, T., Xia, J., 2020. *AIP Advances,* ***10***(12), article no. 125203.
[18] Dütsch, H., Durst, F., Becker, S., Lienhart, H., 1998. *J. Fluid Mech.,* ***360***, pp. 249–271.
[19] Falcucci, G., Jannelli, E., Ubertini, S., Succi, S., 2013. *J. Fluid Mech.,* ***728***, pp. 362–375.
[20] Kaehler, G., Bonelli, F., Gonnella, G., Lamura, A., 2015. *Phys. Fluids,* ***27***(12), article no. 123307.
[21] Nurick, W., 1976. *J. Fluids Eng.-Trans. ASME,* ***98***(4), pp. 681–687.
[22] Soteriou, C., Andrews, R., Smith, M., 1995. "Direct injection diesel sprays and the effect of cavitation and hydraulic flip on atomization". In SAE Technical Paper, no. 950080, SAE International.
[23] Gelalles, A. G., Jan. 1932. Coefficients of discharge of fuel-injection nozzles for compression-ignition engines. NACA Technical Report NACA-TR-373.
[24] Zou, Q., He, X., 1997. *Phys. Fluids,* ***9***(6), pp. 1591–1598.